The B1 shock in the L1157 outflow as seen at high spatial resolution

M. Benedettini, S. Viti, C. Codella, F. Gueth, A. I. Gómez-Ruiz, R. Bachiller, M. T. Beltrán, G. Busquet, C. Ceccarelli, B. Lefloch

Monthly Notices
of the
ROYAL ASTRONOMICAL SOCIETY

MNRAS **436,** 179–190 (2013)
Advance Access publication 2013 September 26

doi:10.1093/mnras/stt1559

The B1 shock in the L1157 outflow as seen at high spatial resolution⋆

M. Benedettini,[1]† S. Viti,[2] C. Codella,[3] F. Gueth,[4] A. I. Gómez-Ruiz,[3] R. Bachiller,[5] M. T. Beltrán,[3] G. Busquet,[1] C. Ceccarelli[6] and B. Lefloch[6]

[1]*INAF-Istituto di Astrofisica e Planetologia Spaziali, via Fosso del Cavaliere 100, I-00133 Roma, Italy*
[2]*Department of Physics and Astronomy, University College London, Gower Street, London WC1E6BT, UK*
[3]*INAF-Osservatorio Astrofisico di Arcetri, Largo E. Fermi 5, I-50125 Firenze, Italy*
[4]*Institut de Radio Astronomie Millimétrique, 300 Rue de la Piscine, F-38406 Saint Martin d'Hères, France*
[5]*Observatorio Astronómico Nacional (IGN), Alfonso XII 3, E-28014 Madrid, Spain*
[6]*UJF-Grenoble 1/CNRS-INSU, Institut de Planétologie et d'Astrophysique de Grenoble UMR 5274, Grenoble F-38041, France*

Accepted 2013 August 16. Received 2013 August 14; in original form 2013 May 21

ABSTRACT

We present high spatial resolution (750 au at 250 pc) maps of the B1 shock in the blue lobe of the L1157 outflow in four lines: CS (3–2), CH_3OH (3_K–2_K), HC_3N (16–15) and p-H_2CO (2_{02}–3_{01}). The combined analysis of the morphology and spectral profiles has shown that the highest velocity gas is confined in a few compact (≈5 arcsec) bullets, while the lowest velocity gas traces the wall of the gas cavity excavated by the shock expansion. A large velocity gradient model applied to the CS (3–2) and (2–1) lines provides an upper limit of 10^6 cm^{-3} to the averaged gas density in B1 and a range of $5 \times 10^3 \leq n_{H_2} \leq 5 \times 10^5$ cm^{-3} for the density of the high-velocity bullets. The origin of the bullets is still uncertain: they could be the result of local instabilities produced by the interaction of the jet with the ambient medium or could be clumps already present in the ambient medium that are excited and accelerated by the expanding outflows. The column densities of the observed species can be reproduced qualitatively by the presence in B1 of a C-type shock and only models where the gas reaches temperatures of at least 4000 K can reproduce the observed HC_3N column density.

Key words: ISM: abundances – ISM: individual objects: L1157 – ISM: jets and outflows – ISM: molecules.

1 INTRODUCTION

Bipolar molecular outflows are one of the easily observable signatures of the early stages of the star formation process producing strong alterations of the protostellar environment both dynamically, accelerating the gas, and chemically, activating the high-temperature chemistry in the shocked gas. One of the most interesting outflows is the one driven by L1157-mm, a low-mass Class 0 protostar located at 250 pc (Looney, Tobin & Kwon 2007). With respect to other outflows driven by low-mass protostars, the L1157 outflow stands out for its rich millimetre spectrum and can be considered as the prototype of chemically active outflows. The outflow has been extensively observed mainly with single-dish telescopes in many molecular lines such as CO (Umemoto et al. 1992; Bachiller et al. 2001), SiO (Zhang et al. 1995; Zhang, Ho & Wright 2000; Nisini et al. 2007), H_2 (Hodapp 1994; Davis & Eislöffel 1995; Neufeld et al. 2009), NH_3 (Tafalla & Bachiller 1995) and CH_3OH (Avery & Chiao 1996). Two main shock events have been detected in the blue lobe of the outflow and the interferometric image of the CO (1–0) line (Gueth, Guilloteau & Bachiller 1996) reveals that they are the apex of two cavities created by the propagation of large bow shocks. The different orientations of the two cavities testify the precession of the driving jet, even if a direct detection of the jet has not yet been obtained. The brightest shock episode, called B1, is located at the apex of the second cavity and has been extensively observed in several molecular species at millimetre (Gueth, Guilloteau & Bachiller 1998; Benedettini et al. 2007; Codella et al. 2009), near-infrared (Nisini et al. 2010a), far-infrared and submillimetre wavelengths (Giannini, Nisini & Lorenzetti 2001; Codella et al. 2010; Lefloch et al. 2010, 2012; Nisini et al. 2010b; Benedettini et al. 2012b), revealing a complex structure with various shock tracers peaking at different positions and the presence of gas at different excitation conditions.

Because of its chemical richness and its clear morphology, the L1157 outflow is an excellent laboratory to study the shock generated by protostellar outflows. Indeed, it was observed by the Chemical Herschel Survey of Star forming regions (CHESS) *Herschel* Key Programme (Ceccarelli et al. 2010) as the prototype

⋆ Based on observations carried out with the IRAM Plateau de Bure Interferometer. IRAM is supported by INSU/CNRS (France), MPG (Germany) and IGN (Spain).

† E-mail: milena.benedettini@inaf.it

Table 1. List of the observed transitions and observing parameters.

Transition	ν (GHz)	E_{up} (K)	Clean beam (arcsec × arcsec)	Resolution (km s^{-1})	rms (mJy beam^{-1})
CH_3OH (3_0–2_0)E	145.094	27.1	3.48 × 2.31 (P.A.=12°)	0.16	20
CH_3OH (3_{-1}–2_{-1})E2	145.097	19.5	3.48 × 2.31 (P.A.=12°)	0.16	20
CH_3OH (3_0–2_0)A^+	145.103	13.9	3.48 × 2.31 (P.A.=12°)	0.16	20
CH_3OH (3_2–2_2)E1, E2	145.126	36.2, 39.8	3.48 × 2.31 (P.A.=12°)	0.16	20
CH_3OH (3_2–2_2)A^+	145.133	35.0	3.48 × 2.31 (P.A.=12°)	0.16	20
HC_3N (16–15)	145.561	59.4	3.47 × 2.30 (P.A.=12°)	1.20	20
p-H_2CO (2_{02}–1_{01})	145.603	10.5	3.47 × 2.30 (P.A.=12°)	1.20	20
CS (3–2)	146.969	14.1	3.43 × 2.25 (P.A.=10°)	0.08	20

of chemically active outflows and it was used to test shock models by many authors (e.g. Gusdorf et al. 2008a; Flower & Pineau des Forêts 2010, 2012). The results of this extensive modelling activity on L1157-B1 testify the complexity of this region where multiple shock types are acting. In fact, different shock tracers have been explained with different types of shocks: a pure C-type shock (Gusdorf et al. 2008a; Neufeld et al. 2009; Viti et al. 2011), a dissociative J-type shock (Benedettini et al. 2012b) and a composition of the two shocks called CJ-type shock (Gusdorf et al. 2008b; Flower & Pineau des Forêts 2010, 2012). However, all the models have been applied to unresolved single-dish data and hence the real structure of the shocked region could not be determined. We have now mapped L1157-B1 with the Plateau de Bure (PdB) interferometer in the 2-mm range, at a spatial resolution of about 3 arcsec corresponding to 750 au at the distance of 250 pc for this source. The observations are described in Section 2. We present the results in Sections 3 and 4, the analysis in Sections 5–7 and the chemical modelling in Section 8. The main conclusions of the paper are summarized in Section 9.

2 OBSERVATIONS

The observations were carried out with the PdB interferometer between 2008 August and 2009 March. The CD configuration was used with three configurations of 5 or 6 antennas. We simultaneously observed the CS (3–2) transition at 146.969 GHz in the lower side band (LSB) and HC_3N (16–15), p-H_2CO (2_{02}–1_{01}) and CH_3OH (3_K–2_K), with frequency between 145.094 and 145.603 GHz in the upper side band (USB). The 20, 40 and 160 MHz correlator units were used for covering different parts of the USB and LSB, resulting in a spectral resolution ranging from 0.08 to 1.2 km s^{-1}. The phase and amplitude calibration was achieved using observations of 1849+670 and 2021+614. The bandpass of the receivers were calibrated using observations of 3C 84 and 3C 454.3. The flux calibration was determined relative to 3C 84 and 3C 454.3, with an uncertainty of 20 per cent. The data were calibrated and analysed with the GILDAS[1] software. Images were produced using natural weighting and were restored with a final clean beam of 3.48 × 2.31 arcsec^2 at 145 GHz. The details of the observations are summarized in Table 1. In particular, the emission at 145.126 GHz is the contribution of two methanol lines, (3_2–2_2)E1 and (3_2–2_2)E2, very close in frequency (145.126191 and 145.126386 GHz) with very similar Einstein coefficients (6.77 × 10^{-6} and 6.86 × 10^{-6} s^{-1}) and upper level energies (36.2 and 39.8 K); therefore, the flux emitted in the two lines should be very similar. We attributed the flux measured at this frequency half to each of the two lines.

[1] http://www.iram.fr/IRAMFR/GILDAS

3 ESTIMATE OF THE FILTERING OF THE LARGE-SCALE EMISSION

With interferometers the largest sensitive structure depends on the shortest baseline which is 14-m for our observations. Hence, our 2-mm observations can only correctly measure the flux of structures smaller than ∼13 arcsec as, for larger structures, part of the flux is missed out. In order to evaluate the missing flux in the lines observed with PdB, we compared the spectrum of each transition produced summing the emission measured at PdB in a circle of diameter equal to the half-power beam width (HPBW) of the IRAM-30 m telescope, with the spectrum measured at the single-dish IRAM-30 m (Gómez-Ruiz et al., in preparation). In Fig. 1, we show the two spectra of the CS (3–2) line. We found that the percentage of the missing flux depends on the velocity: for the high-velocity (HV) gas ($v < -6$ km s^{-1}) PdB recovers 100 per cent of the flux, while for the low-velocity (LV) gas ($v > -6$ km s^{-1}) the flux measured at PdB is ∼62 per cent of the IRAM flux. Similar percentage of missing flux is also found for the other observed lines HC_3N (16–15) and p-H_2CO (2_{02}–1_{01}), while

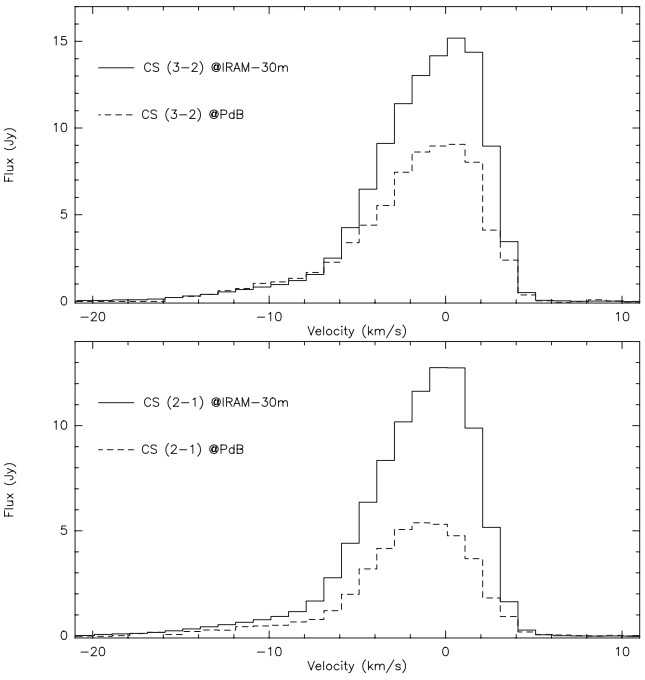

Figure 1. Top: comparison of the CS (3–2) spectrum acquired with the IRAM-30 m (continuum line) (Gómez-Ruiz et al., in preparation) and the equivalent spectrum extracted from the PdB data (dashed line). Bottom: same as the top but for the CS (2–1) line.

for methanol it is not possible to evaluate the missing flux because the lines are blended. We performed the same analysis for the CS (2–1) line previously observed with PdB (Benedettini et al. 2007) with the same CD configuration but a slightly higher value of the shortest baseline (19 m), resulting in a similar value of the largest sensible structure (14 arcsec) and a spatial resolution ($3.11 \times 2.79\,\mathrm{arcsec}^2$) of the 2-mm observations. Unlike the case of the CS (3–2) transition, for the CS (2–1) line the flux filtering affects all the velocities (see Fig. 1). In particular, for the HV gas ($v < -6\,\mathrm{km\,s^{-1}}$) about half (∼50 per cent) of the IRAM flux in the CS (2–1) line is missed in the PdB spectrum, while for $v > -6\,\mathrm{km\,s^{-1}}$ a similar percentage (∼57 per cent) of filtering is measured in the two lines. However, the largest sensitive structure for the CS (2–1) line is similar to the value of the CS (3–2) line; therefore, the difference in the missing flux indicates that a consistent part of the emission of the CS (2–1) line comes from extended (>14 arcsec) structures also for HV gas and therefore is filtered in the PdB spectrum, while the emission of this HV structure in the CS (3–2) line is negligible (see Section 5.1 for further discussion).

4 RESULTS

Line maps of the four observed transitions are shown in Fig. 2. The morphology of the emission is very similar to that observed in other molecules (e.g. Gueth et al. 1998; Benedettini et al. 2007) confirming the clumpy structure superimposed to the more extended arch-like shape seen e.g. in CO (Gueth et al. 1996). It is worth noting that the spatial resolution of these 2-mm maps (∼3 arcsec) is the best compromise for detecting both the extended gas and the compact gas. The clumps B0e, B1a, B1b and B1c, already identified by Benedettini et al. (2007) with previous PdB observations at 3 mm, are clearly present also in these higher energy transitions. It is also worth noting that while the CS and CH_3OH emission have a morphology very similar to that observed in lower excitation lines [with CH_3OH brighter in the west-side clump (B1b) and CS brighter in the east-side clumps (B1a, B1c)], HC_3N and H_2CO are brighter in the north-side clump (B1a), similar to that observed for CH_3CN (8_K–7_K) (Codella et al. 2009). These results confirm the complexity, both in the morphology and in the chemistry, of the B1

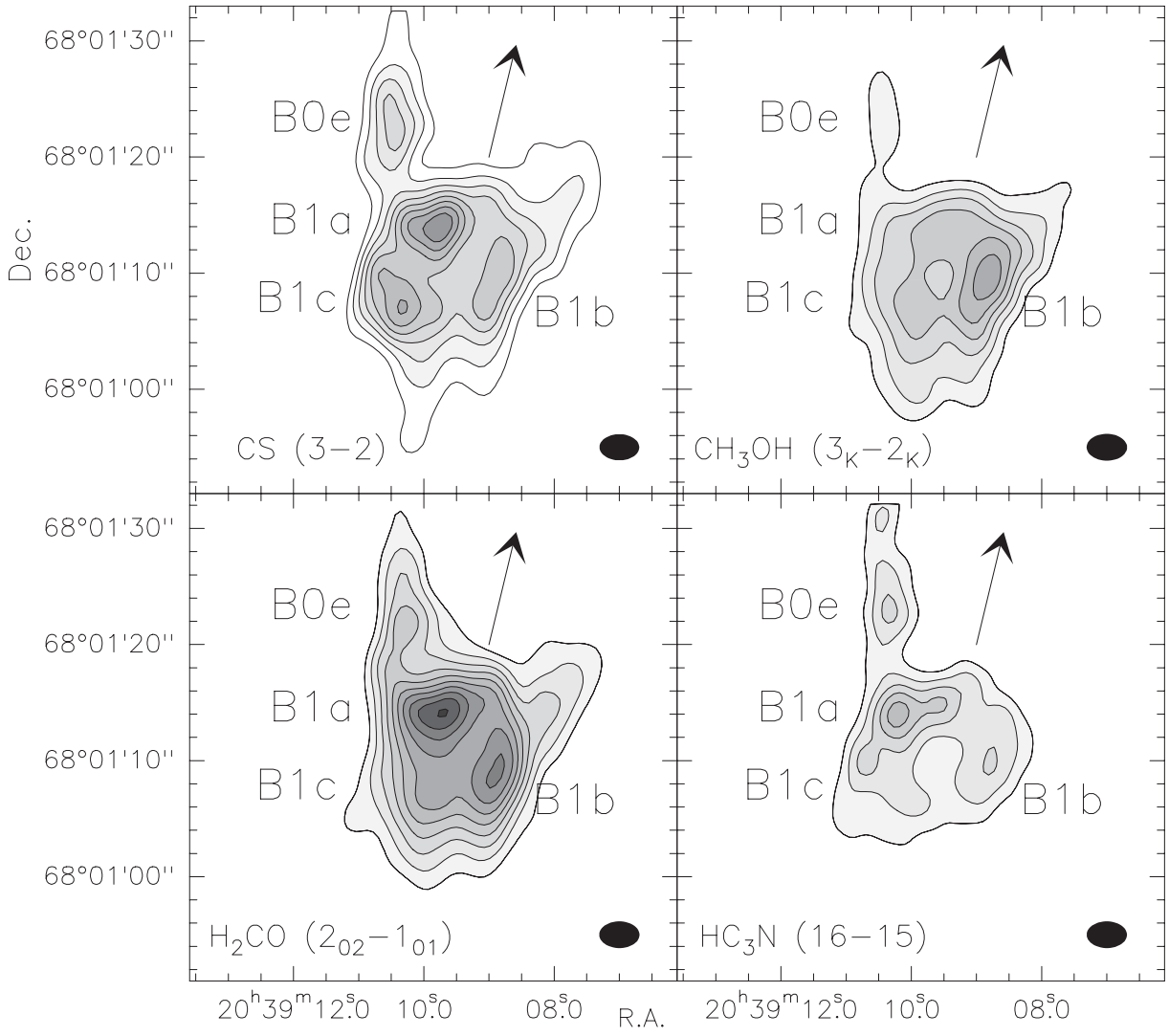

Figure 2. Interferometric images of L1157-B1. The first contour and steps correspond to a 3σ level and are 0.75 Jy beam^{-1} km s^{-1} for CS (3–2), 3 Jy beam^{-1} km s^{-1} for CH_3OH (3_K–2_K), 0.54 Jy beam^{-1} km s^{-1} for p-H_2CO (2_{02}–1_{01}) and 0.15 Jy beam^{-1} km s^{-1} for HC_3N (16–15). The filled ellipse in the bottom left-hand corner represents the HPBW, and the arrow indicates the direction towards the central driving source L1157-mm.

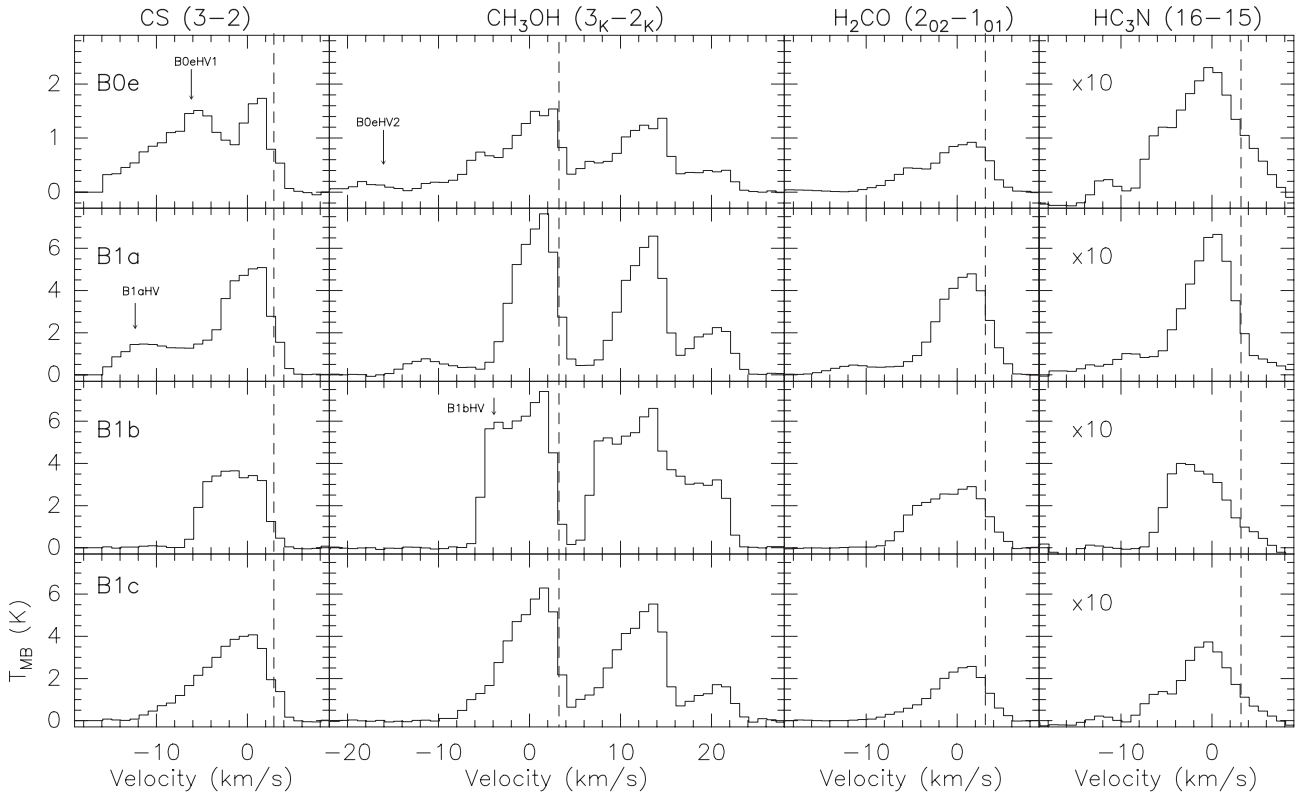

Figure 3. Spectra of the observed lines in the four clumps. The spectra are resampled at a common resolution of $1\,\mathrm{km\,s^{-1}}$. The dashed line indicates the systemic velocity $v_{\rm lsr} = 2.6\,\mathrm{km\,s^{-1}}$. Arrows indicate the peak velocity of the HV bullets. The CH_3OH (3_K–2_K) spectra show three methanol lines and the reference frequency is 145.103185 GHz.

region, likely induced by the shock originated by the interaction between the driving precessing jet and the ambient material.

Differences along B1 are also present in the profiles of the observed lines (see Fig. 3). In most of the observed area, the line emission ends at $\sim+6\,\mathrm{km\,s^{-1}}$ in the red wing and at $\sim-10\,\mathrm{km\,s^{-1}}$ in the blue wing. However, for B0e, B1a and B1b the blue emission extends at velocities lower than $-10\,\mathrm{km\,s^{-1}}$ and the spectra show multiple peaks indicating the presence of different gas components towards these lines of sight. We labelled these spectrally identified additional components flowing at higher velocity with the HV suffix in order to distinguish them from the gas component flowing at velocity closer to the systemic velocity ($2.6\,\mathrm{km\,s^{-1}}$). We found four HV bullets as follows:

(i) in B1a a second peak (called B1a–HV) is detected at $v_{\rm lsr} = -12\,\mathrm{km\,s^{-1}}$; the secondary peak is visible in the spectra of all the observed species;

(ii) in B0e a second peak (called B0e–HV1) is detected at $v_{\rm lsr} = -6\,\mathrm{km\,s^{-1}}$; the secondary peak is visible in the spectra of all the observed species;

(iii) in B0e a third peak (called B0e–HV2) is detected at $v_{\rm lsr} = -16\,\mathrm{km\,s^{-1}}$; this peak is only partially visible in the CS (3–2) spectrum because no data were taken for velocities $<-16\,\mathrm{km\,s^{-1}}$ but it is visible in the CH_3OH spectrum and also in the CS (2–1) (Benedettini et al. 2007);

(iv) in B1b a second peak (called B1b–HV) is detected at $v_{\rm lsr} = -4\,\mathrm{km\,s^{-1}}$; the intensity of the B1b–HV secondary component is similar to the ambient component in all the lines but HC_3N (16–15) where it clearly dominates the emission.

The morphology of B1 at various velocities is shown in the channel maps of Fig. 4. The emission at the line centre (right-hand panels of Fig. 4) clearly shows the walls of the CO cavity and the peaks of the brightest clumps. The emission at intermediate velocities (central panels of Fig. 4) shows still some contributions from the cavity but some clumps emerge (B0e–HV1 at $v_{\rm lsr} = -6\,\mathrm{km\,s^{-1}}$ and B1b–HV at $v_{\rm lsr} = -4\,\mathrm{km\,s^{-1}}$). Finally, the emission at the highest velocities is well confined in only two small clumps: B1a–HV at $v_{\rm lsr} = -12\,\mathrm{km\,s^{-1}}$ and B0e–HV2 at $v_{\rm lsr} = -16\,\mathrm{km\,s^{-1}}$. In Table 2, the position, the peak velocity and the deconvolved size (from 3 to 6 arcsec) of the identified clumps are listed.

Clumpy emission at HV, the so-called extreme HV (EHV) bullets, have been already observed in some outflows driven by low-mass protostars, as, for example, L1148-mm, IRAS 04166+2706 and HH211 (Dutrey, Guilloteau & Bachiller 1997; Gueth & Guilloteau 1999; Nisini et al. 2007; Santiago-García et al. 2009), in the form of a sequence of bullets aligned along the jet that are thought to be associated with episodic ejection events in the jet. Some substantial differences induce us to assert that the HV bullets observed in L1157-B1 are different in nature with respect the EHV bullets. In fact, (i) our bullets have less extreme velocities (from 7 to $19\,\mathrm{km\,s^{-1}}$ with respect to the $v_{\rm lsr}$ of the cloud) than the EHV bullets which have velocity up to $50\,\mathrm{km\,s^{-1}}$; (ii) they are not aligned on a single line along the jet but they have an arch shape and are associated with the walls of the cavity excavated by the jet; (iii) they are chemically rich being observed in several molecular species, while the EHV bullets can only be seen in CO and SiO. Therefore, the L1157-B1 bullets are probably related to local instabilities of the low-excited material swept up by the outflow wind rather than

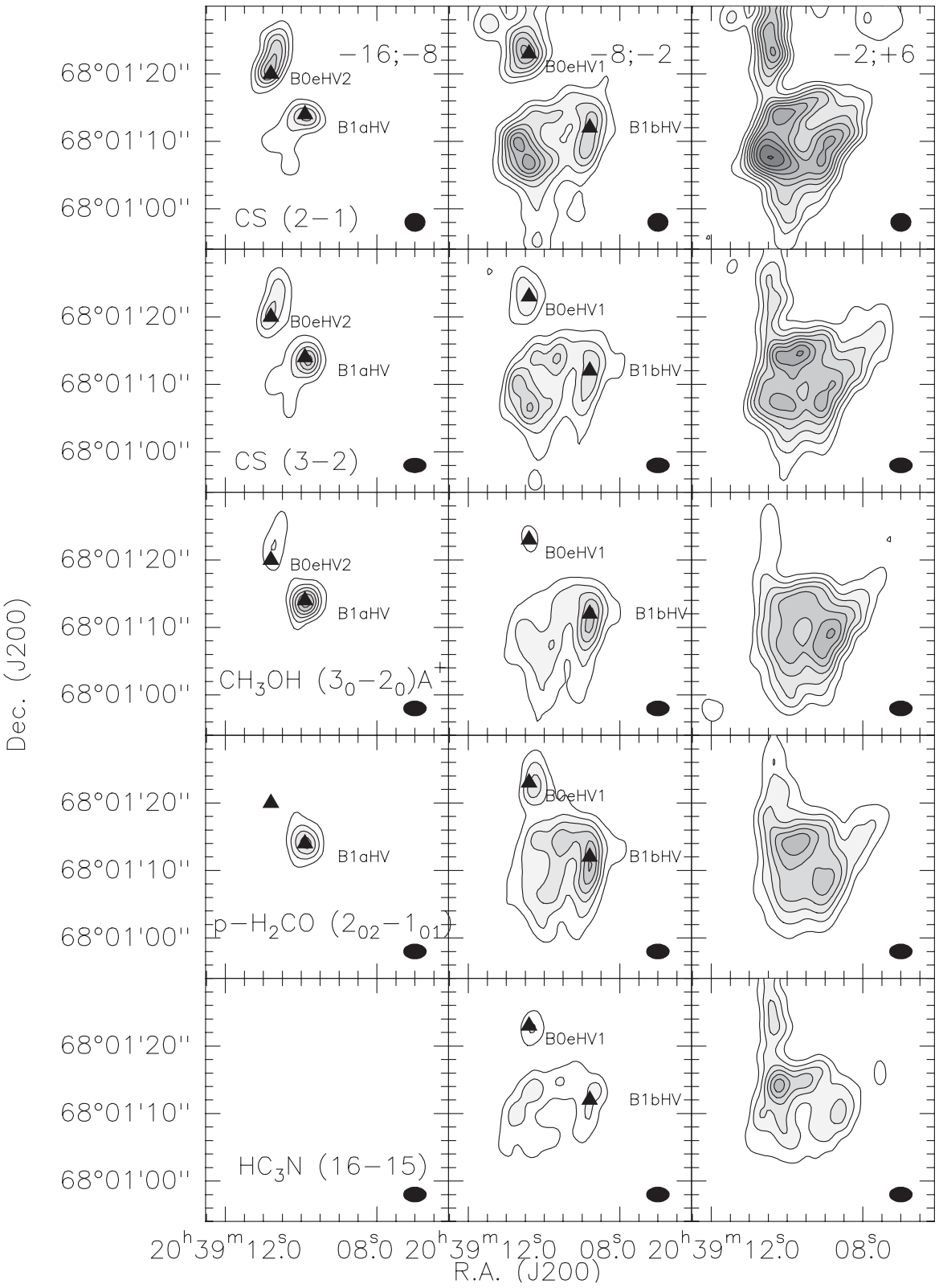

Figure 4. Channel maps of the four observed transitions plus the CS (2–1) (Benedettini et al. 2007). The first contour and contour steps correspond to a 3σ level. Triangles mark the position of the HV bullets. In the left-hand panels the velocity limits are $-16 < v < -8\,\mathrm{km\,s^{-1}}$ and all the flux is recovered, while in the central panels ($-8 < v < -2\,\mathrm{km\,s^{-1}}$) and in the right-hand panels ($-2 < v < +6\,\mathrm{km\,s^{-1}}$) about 60 per cent of the extended emission is filtered out.

Table 2. List of the HV bullets.

Clump	RA (J2000) (h m s)	Dec. (J2000) (° ′ ″)	v(peak) (km s^{-1})	Size (arcsec)
B0e–HV2	20 39 10.8	68 01 20	−16	3
B0e–HV1	20 39 10.6	68 01 23	−6	5
B1a–HV	20 39 09.9	68 01 14	−12	4
B1b–HV	20 39 08.8	68 01 12	−4	6

to local instabilities of the highly excited material of the jet (see Section 7 for further discussion).

5 ANALYSIS OF THE CS LINES

5.1 Lines profiles

Analysing the profile of the CO lines with $J_{up} \leq 16$ observed in L1157-B1 with *Herschel*-Heterodyne Instrument for the Far-Infrared (HIFI), Lefloch et al. (2012) found a common line shape of the CO lines that has been described as a combination of three exponential laws, $I(v) \propto \exp(-|v/v_0|)$. On the basis of their temperature, the authors associated each exponential law to a different gas component of the outflow. In particular, the intermediate-excitation component, called $g2$, with $n_{H_2} \geq 10^5$ cm^{-3} and $T = 64$ K, has been associated with the gas of the walls of the outflow cavity produced by the B1 shock, while the low-excitation component, called $g3$, with $n_{H_2} \geq 10^5$ cm^{-3} and $T = 23$ K, has been associated with the gas belonging to the second cavity of the blue lobe produced by a shock event – B2 – older than B1.

We searched for the same spectral signatures in the CS lines observed with PdB. For the comparison of our data with the *Herschel*-HIFI spectra, we convolved the CS PdB maps to the HIFI spatial resolution at the frequency of the CO (5–4) line, i.e. 37 arcsec, and extracted the spectra over the same beam. Both the CS (2–1) and (3–2) line profiles can be well fitted by a composition of the two exponential laws, $g2$ and $g3$, with the same parameters found for the CO lines (see Fig. 5). This indicates that the CS emission at a large spatial scale, which dominates the line profile in the maps convolved at a higher spatial resolution, arises from the same gas component traced by low- and intermediate-J_{up} CO lines. Our PdB maps show that this large-scale emission originates from the walls of the B1 cavity and therefore confirms the association of $g2$ with the wall of the B1 cavity as suggested by Lefloch et al. (2012). A posteriori we verified that the flux filtering of this extended gas component produced by the interferometer did not modify significantly the line shape. Indeed, the spectral profiles of the two CS (3–2) and (2–1) lines observed with the single-dish IRAM-30 m (Gómez-Ruiz et al., in preparation) are well fitted by the same two exponential laws that fit the PdB spectra convolved at 37-arcsec resolution.

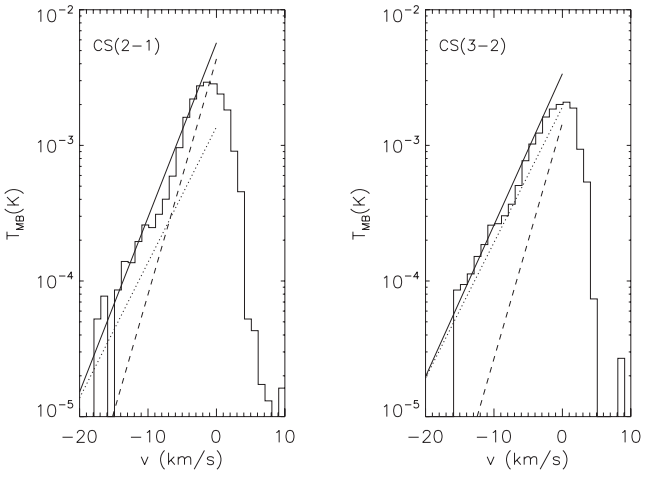

Figure 5. Spectra of the CS (2–1) and (3–2) lines extracted from the PdB maps convolved with a beam of 37 arcsec (the HIFI beam at 576 μm). The spectra are compared with the exponential profiles of the $g2$ (dotted line) and $g3$ (dashed line) components defined by Lefloch et al. (2012). The continuum line is the linear composition of the two exponential fits.

From Fig. 5, we see that for the CS (2–1) line $g2$ and $g3$ provide a similar contribution to the total flux, while the CS (3–2) line is dominated by $g2$, testifying the higher excitation condition of $g2$ with respect to $g3$. Moreover, $g3$ is also associated with a gas at a velocity lower than $g2$; this is a further indication of its association with the slower gas of the older B2 cavity (Benedettini et al. 2007). The gas belonging to the B2 cavity intercepted by the line of sight towards B1 is certainly extended and therefore suffers of filtering in our interferometric observations. In order to quantify this evidence, we calculated the flux of each $g2$ and $g3$ component integrating the two exponential laws in the same velocity range. We found that for $v < -6$ km s^{-1} the $g3$ component in CS (3–2) is 14 per cent of the total flux, while in CS (2–1) it is 40 per cent of the total flux. This result explains the different percentage of the filtering at $v < -6$ km s^{-1} observed in the two CS lines and discussed in Section 3.

5.2 LVG modelling

The physical conditions of the gas component in outflows can be derived by solving the radiative transfer problem in the line simultaneously with the level populations, under the large velocity gradient (LVG) approximation. In this approximation, the line flux depends on the escape probability that is a function of the line optical depth, which in turn is proportional to the number density of the considered molecular species $n(x)$ and is inversely proportional to the velocity gradient dV/dz. Assuming an homogeneous slab where the total velocity dispersion is V, the factor $n(x) \times \mathrm{d}z/\mathrm{d}V$ can be expressed in terms of $N(x)/V$, where $N(x)$ is the column density of the particular molecule, making explicit the dependence of the line flux from the column density. We used the LVG code developed by Ceccarelli et al. (2003) in a plane-parallel geometry using the molecular parameters found in the BASECOL[2] data base (Dubernet et al. 2006). In particular, we modelled the first 31 levels of CS using the collisional coefficients with H_2 from Turner et al. (1992). We adopted a line width of 10 km s^{-1}, as usually done from previous models of this region.

Because of the filtering affecting the extended emission, a quantitative LVG analysis can be carried out for the compact HV gas but not for the diffuse gas component. Nonetheless, we can use the observed CS (3–2)/(2–1) line ratio to provide some general constraints on the physical conditions of the gas. In fact, as shown in Section 3, the filtering affects the CS (2–1) line more than the CS (3–2) line so that the observed line ratio [CS (3–2)/(2–1) = 1.8] can be considered as an upper limit. In Fig. 6, we show the theoretical CS (3–2)/(2–1) line ratio calculated under the LVG approximation. For temperatures higher than ∼60 K, the ratio is quite insensitive to temperature changes and mainly depends on the gas density. However, constraints on the gas temperature can be derived

[2] http://basecol.obspm.fr

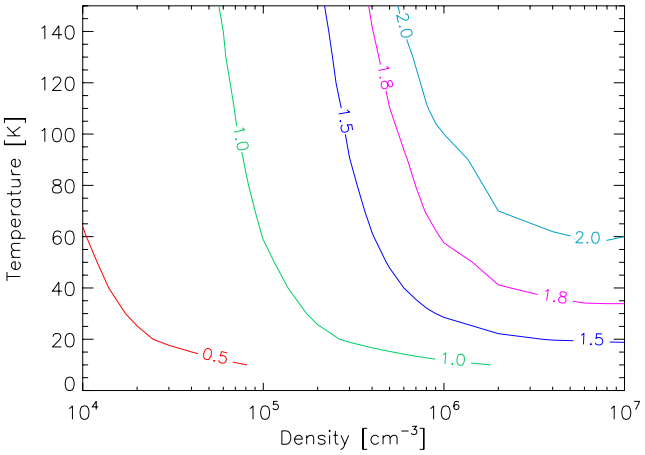

Figure 6. Theoretical CS (3–2)/(2–1) line ratio as a function of density and temperature for a line width of 10 km s^{-1} and a CS column density of 3×10^{13} cm^{-2}, i.e. the typical value derived in B1 (see Table 5). The behaviour of the ratio for column densities in the range 10^{13}–10^{15} cm^{-2} is very similar.

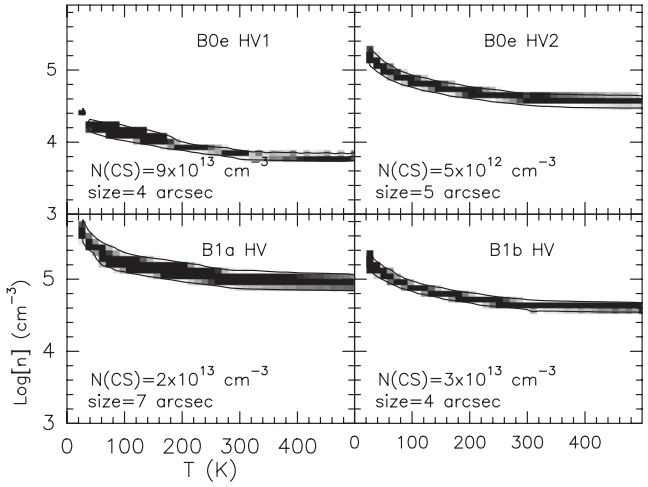

Figure 7. χ^2 distribution in the temperature–density plane for the LVG fitting of the CS lines in the four HV bullets. The black area shows the parameter space with a reduced $\chi^2 \leq 1$ for the CS column density and size written in the panels.

from other tracers. In particular, Codella et al. (2009) measured the temperature in the different B1 clumps by using a rotational diagram of CH_3CN lines observed with PdB in the same configuration of the data of this paper and they found temperatures ranging from 55 to 132 K. This range is compatible with other temperature estimates, namely 80 K derived by Tafalla & Bachiller (1995) by means of Very Large Array observations of NH_3 and 64 K derived by Lefloch et al. (2012) from the CO line observed with *Herschel*-HIFI. For our analysis of L1157-B1, we assume a temperature ranging from 55 to 132 K. Under this constraint, the upper limit of 1.8 for the CS (3–2)/(2–1) line ratio implies an upper limit on the averaged gas density in B1 of 10^6 cm^{-3}. This limit refines previous estimates of the gas density in B1 that provide only a lower limit of $\geq 10^5$ cm^{-3}. In particular, the CO lines from *Herschel* indicate $n_{H_2} \geq 10^5$ cm^{-3}, for the higher excited ($T > 200$ K) gas (Benedettini et al. 2012b; Lefloch et al. 2012). SiO lines indicate $n_{H_2} \geq 3 \times 10^5$ cm^{-3} and $T = 150$–300 K (Nisini et al. 2007). Note however that these lower limits have been derived only from single-dish observations and in some cases from lines with higher excitation temperatures with respect to the ones used in this study.

The compact emission from the HV bullets having size $\lesssim$6 arcsec, lower than the largest sensitive structure ($\sim$14 arcsec) of the interferometer, does not suffer of flux filtering; therefore, we did a quantitative analysis of this emission. In particular, we used the LVG code to derive the physical conditions of the four HV bullets, B0e–HV1, B0e–HV2, B1a–HV and B1b–HV, by using the two CS lines (3–2) and (2–1). In Fig. 4, we show that the HV bullets are detected in both lines. To measure the flux emitted from the HV bullets, we integrated the line emission over the velocity range associated with the specific spectral component. In this way, we are also considering the (minor) contribution of the extended emission that can be present, especially in the spectral component closer to the ambient velocity. However, it is impossible to deblend the flux of the HV bullet from the flux of the more extended component because we do not know the shape of the line profile of the accelerated gas that is not Gaussian. To take into account this additional uncertainty, we associated an error of 20 per cent to the derived line fluxes. In Fig. 7, we show the distribution of the reduced χ^2 as a function of temperature and density for best-fitting values of size and column density. It is well known that CS is a good indicator of the gas density: by using the two CS lines and assuming the size measured in the maps (5 ± 3 arcsec^2), we can constrain quite well the CS column density and the number density of the gas. On the contrary, the temperature remains undefined over a wide range, from a few tens to a few hundreds of kelvin. In Table 3, we report the results of the LVG fitting providing the range of the CS column density and gas density that fit the data under the adopted clump size of (5 ± 3 arcsec^2) and gas temperature (55–132 K). Note that the flux of the CS (3–2) line in B0e–HV2 is underestimated because the spectrum does not cover the whole spectral range of the line. As a consequence the LVG results are approximated and in particular the column density is underestimated. The results of the LVG fitting indicate a lower gas density ($n_{H_2} \leq 10^4$ cm^{-3}) for the B0e–HV1 bullet with respect to the other three bullets ($n_{H_2} \geq 5 \times 10^4$ cm^{-3}). In general, the gas of the HV bullets ($5 \times 10^3 \leq n_{H_2} \leq 5 \times 10^5$ cm^{-3}) seems to be less dense than the large-scale emitting gas ($10^5 \leq n_{H_2} \leq 10^6$ cm^{-3}).

Table 3. Results of the LVG fitting in the HV bullets.

Clump	N(CS) (cm^{-2})	Size (arcsec)	n_{H_2} ($\times 10^4$ cm^{-3})
B0e–HV2	4(12)–1(13)	2–8	5–10
B0e–HV1	6(13)–1(14)	4–8	0.5–1
B1a–HV	2(13)–7(13)	2–8	5–50
B1b–HV	2(13)–8(13)	2–8	2–10

6 CH_3OH ROTATIONAL DIAGRAM

A rough estimate of the gas temperature can be derived by using the rotational diagram. If the emission lines are optically thin, then the slope of the diagram gives directly $1/T_{rot}$ and the rotational temperatures is a lower limit to the kinetic temperature if the gas is not in local thermodynamic equilibrium (LTE).

Since the observed methanol transitions are quite close in frequency in most clumps, the lines are blended (see Fig. 3) and it is not possible to evaluate the contribution of the various spectral components, i.e. the HV clumps. In those cases where it is not possible to deblend the contribution of the HV and LV components, we attributed all the flux at a certain velocity to the dominant component.

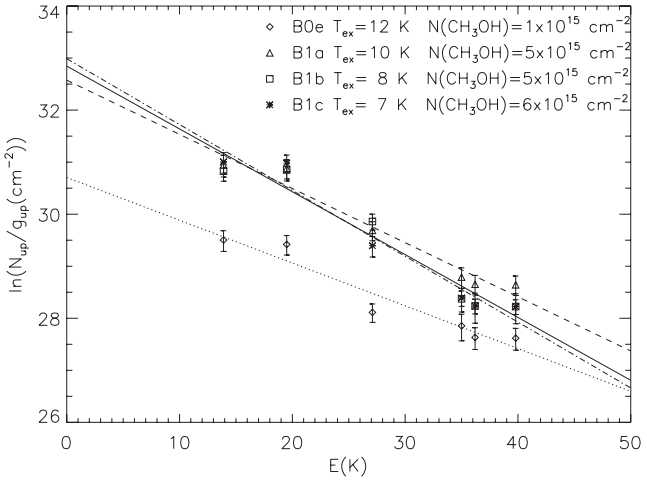

Figure 8. CH_3OH rotational diagrams with superimposed linear fits. Diamonds, triangles, squares and stars correspond to clump B0e, B1a, B1b and B1c, respectively. The inferred excitation temperatures and total CH_3OH column densities for each clump are reported in the figure.

Out of the four HV bullets, only for B1b–HV enough lines can be measured to build the rotational diagram, and we find $T_{\rm rot} = 14$ K and $N(CH_3OH) = 3 \times 10^{15}$ cm^{-2}. We also built the rotational diagrams of the five methanol lines for the LV gas in each clump (see Fig. 8). We find a similar rotational temperature $T_{\rm rot} \simeq 10$ K at all positions, indicating that the excitation conditions are rather uniform in B1. The total column density of CH_3OH is $\simeq 5 \times 10^{15}$ cm^{-2} apart from B0e where it is slightly lower 1×10^{15} cm^{-2}. The derived rotational temperature is in agreement with previous estimates based on single-dish CH_3OH (Bachiller et al. 1995) and $^{13}CH_3OH$ (Codella et al. 2012) data. This quite low temperature indicates that the methanol molecule is subthermally excited. Therefore, $T_{\rm rot} \ll T_{\rm kin}$ and the temperature derived from the rotational diagram cannot be considered as an estimate of the gas kinetic temperature. On the other hand, in the subthermal regime the critical density of the lines provides an upper limit to the gas density. The critical density of the observed methanol lines is of the order of 10^5 cm^{-3}, compatible with the densities of the HV bullets that we found in the previous section from the LVG analysis of CS.

7 ZOOMING IN B0E

In Fig. 9, we plot the CS (3–2) and (2–1) emission from the three spectral components detected towards the B0e region, i.e. the two HV bullets B0e–HV2 at –16 km s^{-1} and B0e–HV1 at –6 km s^{-1} and the LV gas peaking at 1.2 km s^{-1}. The morphology of the three components is very similar in the two lines. As one can see, the position of the peaks of the two highest velocity clumps, B0e–HV1 and B0e–HV2, is external with respect to the walls of the cavity traced by the LV gas. The distance between the peak position of B0e–HV1 and the peak of the LV gas in B0e is 1.4 arcsec, i.e. 1/3 of the spatial resolution of the map, so it may not be significant even if the signal-to-noise ratio of the map is quite good. On the other hand, the distance of the B0e–HV2 with respect to B0e–HV1 and B0e LV is 3.2 and 3.0 arcsec, respectively, i.e. of the same order of the HPBW; hence, it should be a real feature indicating that the compact bullet with the highest velocity is at different position of the slower gas and in particular it is external to the walls of the outflow cavity. In addition, the first moment of both CS lines (Fig. 10) shows a gradient with mean velocity increasing from the

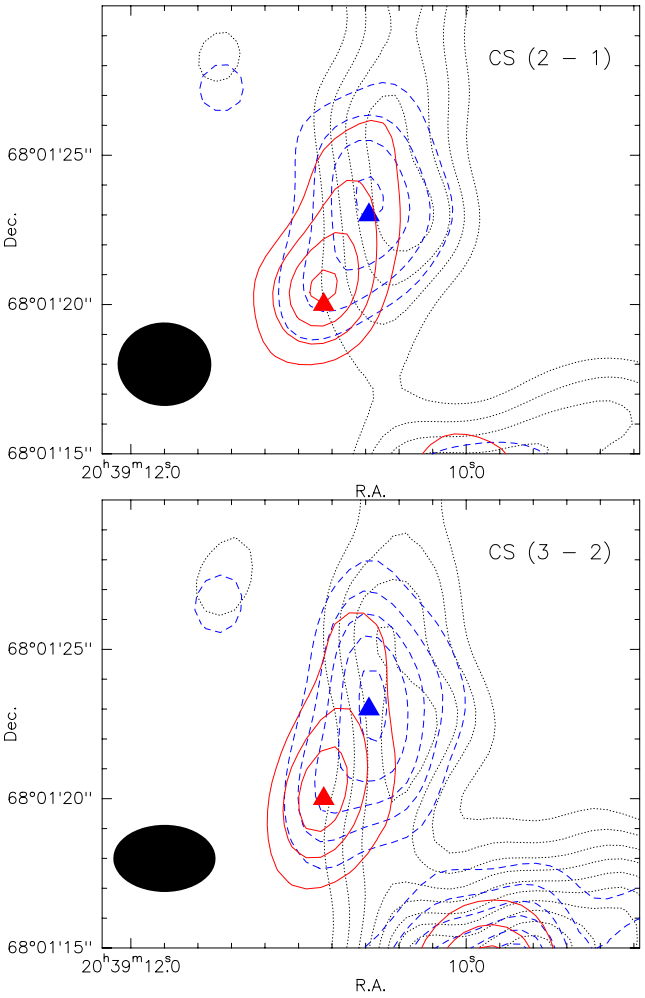

Figure 9. The B0e clump. Top: CS (2–1) line intensity integrated over three velocity ranges: −20.5, −13 km s^{-1} (red solid line) level steps 0.1 Jy beam^{-1} km s^{-1}, −13, −3 km s^{-1} (blue dashed line) first level 0.5 Jy beam^{-1} km s^{-1} steps 0.3 Jy beam^{-1} km s^{-1} and −3, +5 km s^{-1} (black dotted line) first level 0.5 Jy beam^{-1} km s^{-1} steps 0.3 Jy beam^{-1} km s^{-1}. The triangles mark the peak of the emission in each velocity range. The filled ellipse shows the HPBW of the map. Bottom: same as the top but for CS (3–2).

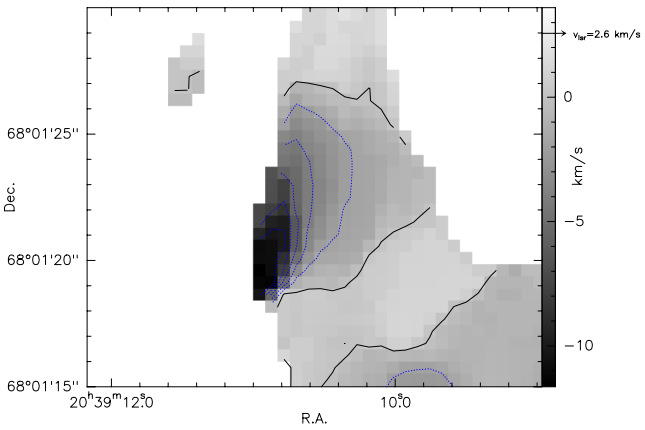

Figure 10. CS (3–2) first moment towards B0e. Continuum line indicates the 0 velocity and dotted lines indicate the negative velocities.

internal wall of the cavity towards the outside in the direction of B0e–HV2.

The interpretation of these very intriguing features is not univocal. It could be the precessing jet that is now impacting at the B0e position producing an acceleration of the gas outwards of the cavity. Presently, there is not any direct detection of the jet driving the L1157 outflow. On the other hand, a large set of shock tracers such as HV SiO (2–1) (Gueth et al. 1998), [Fe II]at 26 μm (Neufeld et al. 2009), H_2 $v = 1$-0 S(1) (Caratti o Garatti et al. 2006), [O I], OH and high-J_{up} CO (Benedettini et al. 2012b) all peak towards B1a, indicating that this is the point with the highest excitation conditions and therefore suggesting that it should be the position where the jet is impacting the lower velocity gas of the outflow. However, the higher gas velocities as well as the velocity gradient in B0e (Fig. 10) seem to imply that the jet is moving towards the B0 position as also foreseen by the model of the jet precession by Gueth et al. (1998). In this scenario, the observed clumpiness could be the result of local instabilities produced by the interaction of the driving jet and the ambient medium. Alternatively, the HV bullets could be clumps already present in the ambient medium before the advent of the outflow that are compressed and pushed by the expanding outflow cavity. The clumpiness of the interstellar medium is well known (e.g. Viti et al. 2003; Morata, Girart & Estalella 2005) and the possible pre-existence of the clumps observed in outflows has been proposed by some authors (Viti et al. 2004a; Benedettini et al. 2006). The slightly lower density that we found in the compact bullets with respect to the bulk of the outflowing gas can support the hypothesis that the clumps are not formed by the outflow but can, at least partially, be present in the cloud before the arrival of the shock and pushed by the shock front. Indeed, from a rough estimate, the momentum of the B0e–HV2 bullet is similar to the momentum of the cavity as expected from the law of the conservation of momentum in collision.

8 THE CHEMISTRY

8.1 Column densities

We estimated the column densities of the observed species towards the clumps by using the same procedure as in Benedettini et al. (2007) for a comparison with the 3 mm set of data. We derived the column density of the detected species in each clump from the integrated intensity of the observed emission lines, assuming LTE condition and that the lines are optically thin. In this case the following formula can be used:

$$N = \frac{8 \times 10^5 \pi k \nu^2}{hc^3 g_{up} A_{ud}} Q(T_{rot}) \exp\left(\frac{E_{up}}{kT_{rot}}\right) \int T_{mb}\, dv, \quad (1)$$

where T_{rot} is the rotational temperature, $Q(T_{rot})$ is the partition function, g_{up} is the degeneracy of the upper level, ν is the frequency of the transition in GHz, A_{ud} is the Einstein coefficient of the transition in s^{-1}, E_{up} is the energy of the upper level of the transition and the integral of the line emission is in K km s^{-1}. The integration limits and the polygon used to calculate the column densities are the same for all molecules in each clump. In Table 4, we list the column densities of the observed molecules assuming the two extreme temperatures of 55 and 132 K. The two values can give an idea of the error associated with the column density produced by the uncertainty on the temperature of the gas. These values must be considered as lower limits because the LTE assumption may be not valid for most of the transitions since they have a critical density $\geq 10^5$ cm^{-3}. Moreover, the total flux of the lines is underestimated due the filtering of the large-scale emission (see Section 3).

Considering the large uncertainty in the column densities derived with such a procedure, which can be as high as one order of magnitude, we can say that the values derived from the present 2-mm data are consistent with the ones previously derived from 3-mm data

Table 4. Column density of the observed species calculated in each clump for two different temperatures. The notation used is a(b) that means a $\times 10^b$.

Clump	Transition	Flux (K km s^{-1})	$N(X_i)$ ($T = 55$ K) (cm^{-2})	$N(X_i)$ ($T = 132$ K) (cm^{-2})
B0e	CS (3–2)	18.9	4.6(13)	9.4(13)
B1a	CS (3–2)	33.1	8.0(13)	1.6(14)
B1b	CS (3–2)	24.9	6.1(13)	1.2(14)
B1c	CS (3–2)	28.8	8.0(13)	1.4(14)
B0e	CH_3OH (3_1–2_1)E	1.8	8.8(14)	2.2(15)
B1a	CH_3OH (3_1–2_1)E	3.7	1.9(15)	4.7(15)
B1b	CH_3OH (3_1–2_1)E	6.0	3.0(15)	7.4(15)
B1c	CH_3OH (3_1–2_1)E	2.4	1.2(15)	3.0(15)
B0e	CH_3OH (3_0–2_0)A^+	11.8	3.6(15)	1.1(16)
B1a	CH_3OH (3_0–2_0)A^+	36.8	1.1(16)	3.6(16)
B1b	CH_3OH (3_0–2_0)A^+	48.1	1.5(16)	4.6(16)
B1c	CH_3OH (3_0–2_0)A^+	33.9	1.0(16)	3.3(16)
B0e	p-H_2CO (2_{02}–1_{01})	11.2	3.2(14)	1.0(15)
B1a	p-H_2CO (2_{02}–1_{01})	27.7	8.0(14)	2.6(15)
B1b	p-H_2CO (2_{02}–1_{01})	23.3	6.7(14)	2.2(15)
B1c	p-H_2CO (2_{02}–1_{01})	16.0	4.6(14)	1.2(15)
B0e	HC_3N (16–15)	2.2	2.6(13)	3.3(13)
B1a	HC_3N (16–15)	3.6	4.2(13)	5.3(13)
B1b	HC_3N (16–15)	2.6	2.9(13)	3.7(13)
B1c	HC_3N (16–15)	2.4	2.7(13)	3.5(13)

Table 5. Molecular column densities in the HV clumps assuming a $T = 64$ K.

Clump	$N(HC_3N)$ (cm^{-2})	$N(H_2CO)$ (cm^{-2})	$N(CH_3OH)$ (cm^{-2})	$N(CH_3OH)$ [a] (cm^{-2})	$N(CS)$ (cm^{-2})	$N(CS)$[b] (cm^{-2})
B0e–HV2	–	1×10^{13}	3×10^{14}	–	$>4 \times 10^{12}$	$>4 \times 10^{12}$
B0e–HV1	6×10^{12}	6×10^{13}	1×10^{15}	–	3×10^{13}	9×10^{13}
B1a–HV	4×10^{12}	7×10^{13}	1×10^{15}	–	2×10^{13}	2×10^{13}
B1b–HV	1×10^{13}	2×10^{14}	5×10^{15}	3×10^{15}	2×10^{13}	3×10^{13}

[a]Derived from rotational diagram.
[b]Derived from the LVG modelling.

(Benedettini et al. 2007), the two differing no more than a factor of 10.

We also calculated the column density of the HV bullets by using equation (1) and assuming a temperature of 64 K. The results are presented in Table 5 where also the values of CS and CH_3OH column densities derived with other methods are reported (see Sections 5.2 and 6). For each of the observed species, the column densities in the four HV bullets are similar. In addition, there are also no large differences between the column densities of the bullets (Table 5) and the column densities of the emission at larger scales (Table 4).

8.2 Comparison with chemical shock models

We compared the observed column densities of the HV bullets with chemical models of C-type shock previously used in Viti et al. (2011) for modelling the $H_2O(1_{10}–1_{01})$ and NH_3 ($1_0–0_0$) lines in L1157-B1. The models were run with a code that couples the UCL_CHEM time-dependent gas–grain chemical code (Viti et al. 2004b) with the parametric shock model of Jiménez-Serra et al. (2008) which calculates the physical structure of a plane-parallel steady-state C-shock that propagates through an unperturbed medium. We refer to Viti et al. (2011) for the detailed description of the model and the choice of the investigated parameter space. We analysed the same parameter space as in Viti et al. (2011) using all the models of their table 1.

In Fig. 11, we show the evolution of the chemical abundances with respect to H_2 as a function of distance within the shock. For a direct comparison of our data with the models, we calculated the theoretical column density of the observed species summing the contribution of the gas along the length of the shock (see Fig. 12). Because of the inclination of the L1157 outflow, these calculated values correspond to the column densities along the line of sight only in the case of a spherical symmetry of the shocked area. Any deviation of the real shock geometry from the spherical symmetry introduces errors in the theoretical column density. However, the large uncertainties on the observed column densities, which can be as high as one order of magnitude, make useless a comparison with a more complex model of the geometry.

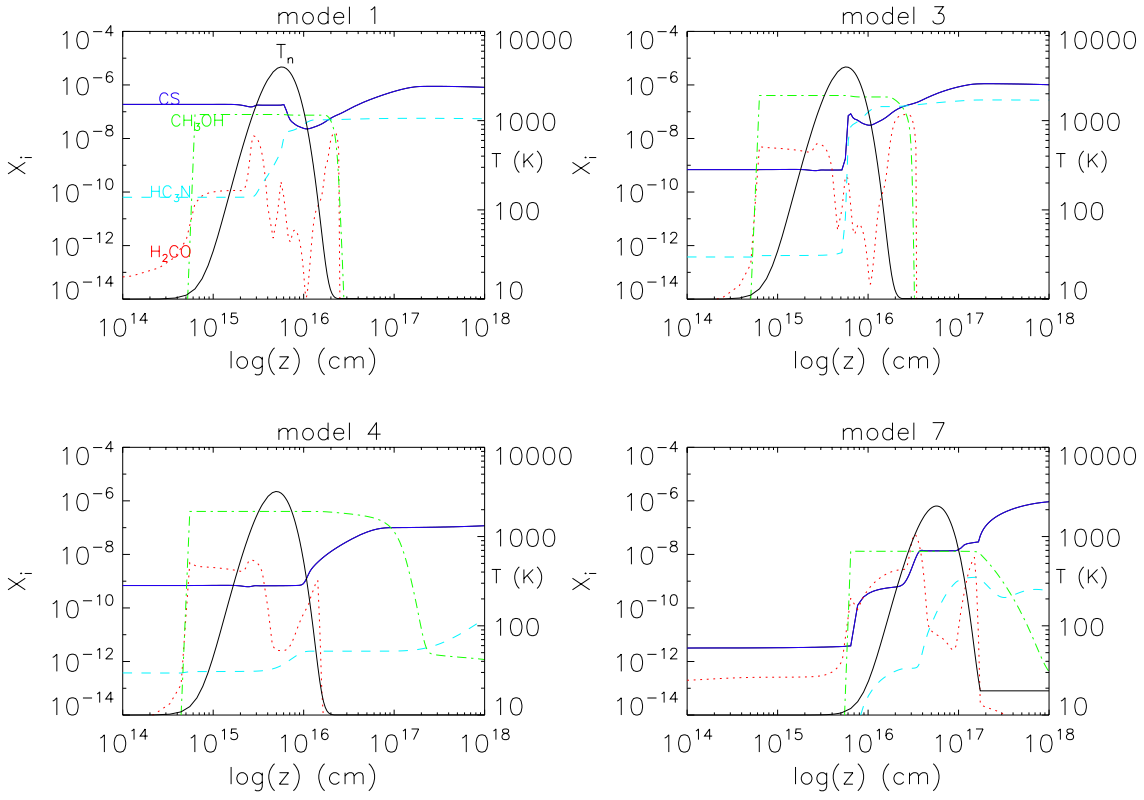

Figure 11. Fractional chemical abundances with respect to H_2 versus the distance as predicted by the Viti et al. (2011) models: continuum blue for CS, dot–dashed green for CH_3OH, dashed cyan for HC_3N and dotted red for H_2CO. The temperature profile (black) for each model is also shown.

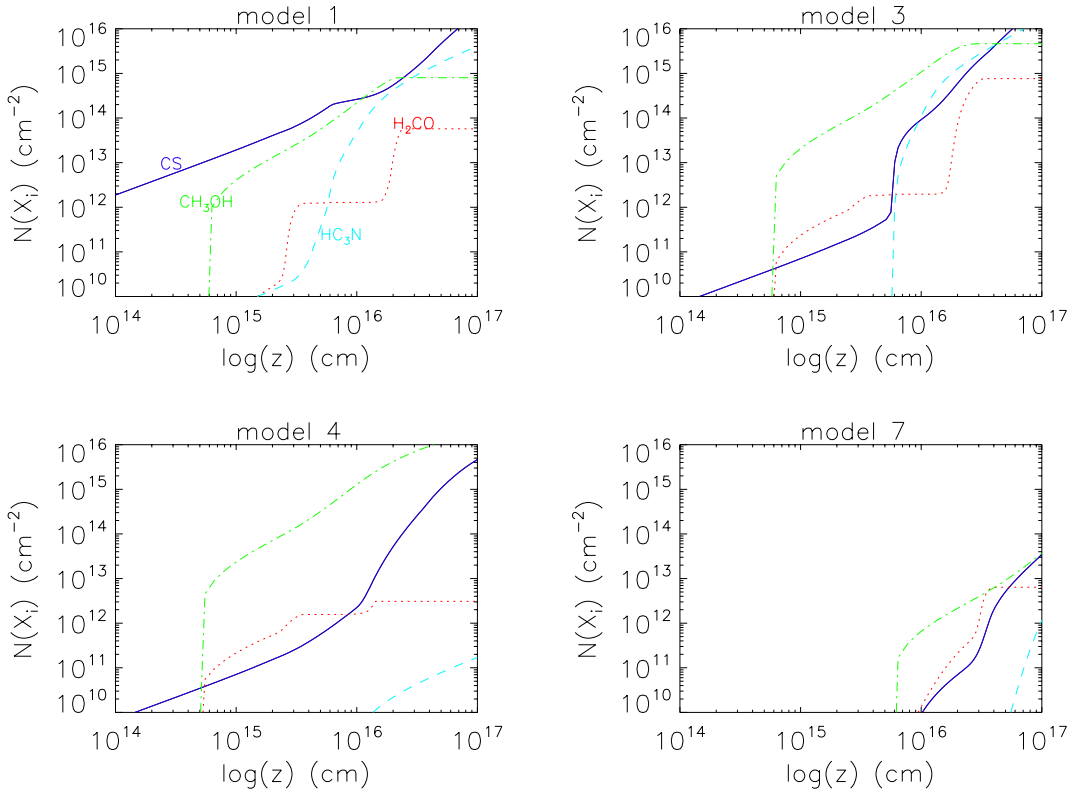

Figure 12. Column densities of the observed species versus distance as predicted by the Viti et al. (2011) models: continuum blue for CS, dot–dashed green for CH_3OH, dashed cyan for HC_3N and dotted red for H_2CO.

At the distance of L1157-B1 (250 pc; Looney et al. 2007), the average dimension of the HV clump of 5 arcsec corresponds to a size of 2×10^{16} cm, while the total dimension of B1 in our maps is ∼20 arcsec, corresponding to about 8×10^{16} cm, and it should be considered as a lower limit because of the filtering of the large-scale emission in interferometer (see Section 2.1). On the other hand, the upper limit for the size of B1 can be derived from IRAM-30 m single-dish observations (Bachiller et al. 2001) to be 30 arcsec, corresponding to about 10^{17} cm; hence, in Fig. 12 we limit the *x*-axis to that size. We find that models with low pre-shock density (10^3 cm^{-3}) have long saturation time resulting in shock length larger than 3×10^{17} cm which corresponds to an angular size larger than the total dimension of the blue lobe of L1157, while models with pre-shock density larger than 10^4 cm^{-3} are compatible with the dimension of the B1 shock. In particular, for models with pre-shock density of 10^5 cm^{-3} the column densities integrated over a linear dimension of $\sim 10^{17}$ cm include both the thin shock layer at high temperature and the post-shocked region where the temperature drops.

Models show that CH_3OH and H_2CO, species mainly formed on the grains, are sputtered back to the gas phase as soon as the shock temperature increases to a few tens of kelvin. Therefore, the abundance of these species is not directly linked to the parameters of the shock but mainly depends on the percentage of gas depleted on to the dust grains during the cold pre-shock phase. In general, models with a low percentage of depletion (<30 per cent of gas-phase CO frozen on to grains at the end of the accretion phase) produce the column density of CH_3OH and H_2CO a few orders of magnitude lower than observed (see, for example, model 1). It is interesting to note, however, that H_2CO has a double-peak behaviour (see Fig. 11), with the first peak occurring when the temperature starts to increase; as the shock progresses formaldehyde starts declining; it then increase again once the shock has passed through and the gas cools down. This behaviour is explained by the fact that the dominant route of destruction for this species is via a reaction with atomic hydrogen, whose abundance is directly proportional to the temperature.

Also of particular interest is HC_3N, a molecule that has never been analysed before in the framework of shock models in protostellar outflows. In fact, HC_3N has been observed and modelled in many pre-stellar core with fractional abundances from a few $\times 10^{-10}$ up to 6×10^{-8} in TMC-1 Core D (e.g. Ohishi & Kaifu 1998; Tafalla et al. 2006). However, Benedettini et al. (2012a) showed that in pre-stellar cores, HC_3N is quickly destroyed once the main accretion phase is finished. Beltrán et al. (2004) observed HC_3N (12–11) along the wall of the cavity of the L1157 outflow close to the driving protostar and claimed that the enhancement of HC_3N could be produced by the shock created by the precessing jet. Indeed, in our shock models we find that this species is formed during the shock, and only models where the gas reaches high maximum temperatures ($T_{max} = 4000$ K) can reproduce the observed HC_3N column density: HC_3N formation is enhanced at high temperatures mainly because of the reaction: $C_2H + HCN$ which forms HC_3N. This reaction has a barrier of 770 K (Hoobler & Leone 1997; Woodall et al. 2007). Therefore, it is clear that the higher the temperature the more efficient HC_3N formation is. In order to reach the observed abundance, and considering the short-lived high-temperature phase, models with a high T_{max} are favoured, in agreement with the conclusions drawn in Viti et al.

(2011) for ammonia. It is possible of course that this species would be equally enhanced in models where a lower, but longer lived, temperature phase is maintained.

In conclusions, in agreement with Viti et al. (2011), we find that the observed column densities in L1157-B1 can be reproduced qualitatively by the presence of a C-type shock with a pre-shock density $n_{H_2} > 10^4\,cm^{-3}$ and velocity $\sim 40\,km\,s^{-1}$, so that the maximum shock temperature reaches the 4000 K.

9 CONCLUSIONS

We present high spatial resolution maps of the B1 shock knot in the blue lobe of the L1157 outflow of the CS (3–2), CH_3OH (3_K–2_K), HC_3N (16–15) and p-H_2CO (2_{02}–3_{01}) lines. The combined analysis of the morphology and spectral profiles has shown that the gas flowing at higher velocity is confined to a few compact ($\approx$5 arcsec) bullets, while the gas flowing at lower velocity traces the wall of the gas cavity excavated by the jet and the apex of the B1 bow shock. In particular, two HV bullets, one peaking at $-16\,km\,s^{-1}$ and one peaking at $-6\,km\,s^{-1}$, have been detected in the direction of the north-east B0e clump; one HV bullet at $-12\,km\,s^{-1}$ has been detected in the direction of B1a and one at $-4\,km\,s^{-1}$ in the direction of B1b.

We applied an LVG model to the CS (3–2) and (2–1) lines whose ratio is a good tracer of the gas density. Using temperature estimate from the literature, we were able to provide an upper limit of $10^6\,cm^{-3}$ to the B1-averaged gas density, therefore refining previous density estimates that provide only a lower limit of $10^5\,cm^{-3}$. For the compact bullets, we found that the gas density is in the range of $5 \times 10^3 \leq n_{H_2} \leq 5 \times 10^5\,cm^{-3}$; therefore, they seem to be less dense than the large-scale emitting gas.

We derived the column densities of the observed species both for the large-scale gas and the compact gas, and we found similar values. In particular, the observed column densities in L1157-B1, derived from low/medium energy transitions ($E_{up} < 60$ K) of the four molecules CS, CH_3OH, HC_3N and H_2CO, can be reproduced qualitatively by the presence in B1 of a C-type shock with a pre-shock density $n_{H_2} > 10^4\,cm^{-3}$. The measured enhancement of the HC_3N abundance requires a maximum shock temperature of at least 4000 K that can be reached for shock velocity of $\sim 40\,km\,s^{-1}$.

Of particular interest is the B0e region where we found a gradient of the first moment with increasing velocity moving from the internal wall of the cavity towards the outside in the direction of B0e–HV2, the higher velocity bullet that is external with respect to the walls of the outflow cavity. The interpretation of this very intriguing feature is not univocal: it may be that the precessing jet, not yet observed directly in the L1157 outflow, is now impacting at the B0e position accelerating the gas outwards of the cavity, or alternatively that the compact HV bullet is a clumpy structure formed, at least partially, before the advent of the outflow as suggested by the lower gas density in the HV bullets.

ACKNOWLEDGEMENTS

GB and AIG-R are supported by an Italian Space Agency (ASI) fellowship under contract number I/005/11/0.

REFERENCES

Avery L. W., Chiao M., 1996, ApJ, 312, 788
Bachiller R., Liechti S., Walmsley C. M., Colomer F., 1995, A&A, 295, L51
Bachiller R., Pérez Gutiérrez M., Kumar M. S. N., Tafalla M., 2001, A&A, 372, 899
Beltrán M. T., Gueth F., Guilloteau S., Dutrey A., 2004, A&A, 416, 631
Benedettini M., Yates J. A., Viti S., Codella C., 2006, MNRAS, 370, 229
Benedettini M., Viti S., Codella C., Bachiller R., Gueth F., Beltran M. T., Dutrey A., Guilloteau S., 2007, MNRAS, 381, 1127
Benedettini M., Pezzuto S., Burton M. G., Viti S., Molinari S., Caselli P., Testi L., 2012a, MNRAS, 419, 238
Benedettini M. et al., 2012b, A&A, 539, L3
Caratti o Garatti A., Giannini T., Nisini B., Lorenzetti D., 2006, A&A, 449, 1077
Ceccarelli C., Maret S., Tielens A. G. G. M., Castets A., Caux E., 2003, A&A, 410, 587
Ceccarelli C. et al., 2010, A&A, 521, L22
Codella C. et al., 2009, A&A, 507, L25
Codella C. et al., 2010, A&A, 518, L112
Codella C. et al., 2012, ApJ, 757, L9
Davis C. J., Eislöffel J., 1995, A&A, 330, 851
Dubernet M.-L., Grosjean A., Flower D., Roueff E., Daniel F., Moreau N., Debray B., 2006, J. Plasma Res. Ser., 7, 356
Dutrey A., Guilloteau S., Bachiller R., 1997, A&A, 325, 758
Flower D. R., Pineau des Forêts G., 2010, MNRAS, 406, 1745
Flower D. R., Pineau des Forêts G., 2012, MNRAS, 421, 2786
Giannini T., Nisini B., Lorenzetti D., 2001, ApJ, 555, 40
Gueth F., Guilloteau S., 1999, A&A, 343, 571
Gueth F., Guilloteau S., Bachiller R., 1996, A&A, 307, 891
Gueth F., Guilloteau S., Bachiller R., 1998, A&A, 333, 287
Gusdorf A., Cabrit S., Flower D. R., Pineau des Forêts G., 2008a, A&A, 482, 809
Gusdorf A., Pineau des Forêts G., Cabrit S., Flower D. R., 2008b, A&A, 490, 695
Hodapp K.-W., 1994, ApJS, 94, 615
Hoobler R. J., Leone S. R., 1997, J. Geophys. Res., 102, 281617
Jiménez-Serra I., Caselli P., Martín-Pintado J., Hartquist T. W., 2008, A&A, 482, 549
Lefloch B. et al., 2010, A&A, 518, L113
Lefloch B. et al., 2012, ApJ, 757, L25
Looney L. W., Tobin J. J., Kwon W., 2007, ApJ, 670, L131
Morata O., Girart J. M., Estalella R., 2005, A&A, 435, 113
Neufeld D. A. et al., 2009, ApJ, 706, 170
Nisini B., Codella C., Giannini T., Santiago García J., Richer J. S., Bachiller R., Tafalla M., 2007, A&A, 462, 163
Nisini B., Giannini T., Neufeld D. A., Yuan Y., Antoniucci S., Bergin E. A., Melnick G. J., 2010a, ApJ, 724, 69
Nisini B. et al., 2010b, A&A, 518, L120
Ohishi M., Kaifu J., 1998, Faraday Discuss., 109, 205
Santiago-García J., Tafalla M., Johnstone D., Bachiller R., 2009, A&A, 495, 169
Tafalla M., Bachiller R., 1995, ApJ, 443, L40
Tafalla M., Santiago-García J., Myers P. C., Caselli P., Walmsley C. M., Craspi A., 2006, A&A, 455, 577
Turner B. E., Chan Kin-Wing, Green S., Lubowich D. A., 1992, ApJ, 399, 114
Umemoto T., Iwata T., Fukui Y., Mikami H., Yamamoto S., Kameya O., Hirano N., 1992, ApJ, 392, L83
Viti S., Girart J. M., Garrod R., Williams D. A., Estalella R., 2003, MNRAS, 399, 187
Viti S., Codella C., Benedettini M., Bachiller R., 2004a, MNRAS, 350, 1029
Viti S., Collings M. P., Dever J. W., McCoustra M. R. S., Williams D. A., 2004b, MNRAS, 354, 1141
Viti S., Jimenez-Serra I., Yates J. A., Codella C., Vasta M., Caselli P., Lefloch B., Ceccarelli C., 2011, ApJ, 740, L3
Woodall J., Agndez M., Markwick–Kemper A. J., Millar T. J., 2007, A&A, 466, 1197
Zhang Q., Ho P. T. P., Wright M. C. H., Wilner D. J., 1995, ApJ, 451, L71
Zhang Q., Ho P. T. P., Wright M. C. H., 2000, ApJ, 119, 1345

This paper has been typeset from a TEX/LATEX file prepared by the author.